ELSEVIER

European Journal of Cancer 41 (2005) 1073–1085

European Journal of Cancer

www.ejconline.com

Long-term observation reveals time-course-dependent characteristics of tumour vascularisation

Nils Hansen-Algenstaedt [a,b,*], Claudia Joscheck [a,b], Christian Schaefer [a,b], Katrin Lamszus [c], Lars Wolfram [a,b], Tanja Biermann [a,b], Petra Algenstaedt [d], Marc A. Brockmann [c], Carsten Heintz [e], Walter Fiedler [f], Wolfgang Rüther [a,b]

[a] *Department of Orthopedic Surgery, University Hospital Hamburg-Eppendorf, Martinistr. 52, 20246 Hamburg, Germany*
[b] *Department of Center of Biomechanics, University Hospital Hamburg-Eppendorf, Martinistr. 52, 20246 Hamburg, Germany*
[c] *Department of Neurosurgery, University Hospital Hamburg-Eppendorf, Martinistr. 52, 20246 Hamburg, Germany*
[d] *Department of Internal Medicine, University Hospital Hamburg-Eppendorf, Martinistr. 52, 20246 Hamburg, Germany*
[e] *Department of Vascular and Abdominal Surgery, AK Harburg, Hamburg, Germany*
[f] *Department of Oncology and Haematology, University Hospital Hamburg-Eppendorf, Martinistr. 52, 20246 Hamburg, Germany*

Received 15 December 2004; accepted 16 December 2004
Available online 14 April 2005

Abstract

Functional properties of tumour vasculature influence the process of metastasis and play a role in generating a heterogeneous metabolic microenvironment, which contributes to genetic instability and inefficiency of tumour therapies. Morphological and functional properties of tumour vasculature may vary from tumour onset to late-stage disease. The aim of this study was to identify the dynamic alteration in tumour microcirculation in a chronic observation model. Invasively-growing, non-disseminating, green fluorescent protein transfected, human bone marrow derived endothelial cells, were implanted into cranial windows of severe combined immunodeficient mice. Intravital fluorescence microscopy was performed over a period of 85 days to measure permeability, leucocyte–endothelial interaction (LEI) and tissue perfusion rate as functional parameters. Vessel density, branching pattern and scanning electron microscopy were monitored as morphological parameters. Concordant with an increasing count of transendothelial pores, the results show that the initial event following tumour cell implantation was a significant increase in the permeability of pre-existing vessels. The variations in newly formed vessels were characterised by sequentially-occurring functional and morphological alterations with the development of characteristics typical of tumour vessels, such as increased count of trifurcations and variation in vessel calibre by more than 100%. In parallel with the increasing vessel volume per area, the tissue perfusion rate increased until day 61. It is concluded from the step-specific sequential functional and morphological alterations that the efficiency of adjuvant therapies depends not only on their intrinsic efficiency but also on the timing of their initiation.

Keywords: Angiogenesis; Microcirculation; Drug delivery; Intravital microscopy

1. Introduction

Functional properties of the tumour vasculature are critical for the progression of tumours [1]. They are decisive for organ-specific metastasis [2,3] and genetic instability of hypoxic regions [4] as well as for the efficiency of tumour therapy (e.g., drug delivery to solid tumours) [5]. Therapies targeting new vessel formation and modulating vascular functions have, therefore, become a promising therapeutic approach for the treatment of malignancies [6,7]. Yet, from the unsatisfactory results of clinical translation into anti-angiogenic therapies

* Corresponding author. Tel.: +40 42 80 36 567; fax: +40 42 80 34 991.
E-mail address: nhansen@uke.uni-hamburg.de (N. Hansen-Algenstaedt).

0959-8049/$ - see front matter © 2005 Elsevier Ltd. All rights reserved.
doi:10.1016/j.ejca.2004.12.034

[8–10], it became apparent that, despite enormous insights into the molecular mechanisms of tumour vessel formation, the multifaceted, time-course-dependent properties of tumour vascularisation [11] represent an inexorable problem to successful anti-angiogenic therapies.

The process of new vessel formation is characterised by sequential alteration in vascular functions associated with the stepwise angiogenic process [12]. Unravelling such step-specific alterations might lead to the possibility of step-specific therapeutic interventions [13] exploiting the functional characteristics to ameliorate existing therapies or to development of new therapeutic strategies [14].

Microvessels of normal tissues form a regular vascular network with a tissue-specific structure, branching pattern and size-range. They are distributed at regular and closely spaced intervals (100 μm), resulting in sufficient exchange of gases, ions and other molecules for tissue nutrition and waste removal.

Tumour vessels differ markedly from the normal vascular architecture in their organisation, structure and function. They exhibit a serpentine course, branch irregularly and form arterio-venous shunts. Vessels that supply tumour tissue are characterised by a non-uniform distribution, resulting in relatively normal and underperfused regions in direct neighbourhood [15,16] causing the heterogeneity of the microenvironment that contributes to drug resistance [4,17]. Tumour vessels often lack innervation and the hierarchical pattern found in normal vascularised tissue with arterioles, capillaries and venules [18]. Due to their abnormal structure, the function of tumour vessels is altered. Blood flow is characterised by temporal and local heterogeneity, leading to lower blood perfusion rates in tumours than in normal tissues [19]. Because of the serpentine course of tumour vessels, their thin walls, increased interstitial pressure and local factors, the geometric resistance differs markedly from normal tissue. Increased vessel diameter and viscosity reduce tumour blood flow, whereas elevation of viscosity is due to an increased haematocrit by hyperpermeability and plasma leakage as well as decreased blood flow velocity itself [20].

Although microvascular properties are of central importance in both tumour progression (e.g., metastasis) and tumour therapy [12,21], the time course of the development of these tumour vessel characteristics from tumour onset until late-stage disease remains enigmatic. Detailed insights into the time course of functional and morphological properties are a prerequisite for therapies targeting or exploiting vascular properties. The aim of this study was to identify and characterise dynamic morphological and functional alterations of tumour microcirculation in a chronic observation model.

This article examines the alterations of functional and morphological vascular parameters of pre-existing and tumour vessels from tumour onset until late-stage tumour disease to gain insights into the dynamics of tumour vascularisation and their potential contribution to the development of barriers to drug delivery. Intravital microscopy was carried out, to allow non-invasive and continuous monitoring, using scanning electron microscopy to correlate functional parameters with anatomical aspects.

2. Material and methods

2.1. Tumour model

A human bone marrow derived endothelial cell line (GFP-transfected, HBMEC-1) [22,23] was implanted in cranial windows [24] of 12-week-old, male, severe combined immunodeficient (SCID) mice from our gnotobiotic colony. A cell suspension of 0.5×10^6 HBMEC-1 cells in 4 μl of nutrition media was used to implant the tumour cells on the cranial hemispheres before closing with a glass cover-slip for non-invasive and continuous intravital microscopy. Because the focus of the study was a long-term observation of morphological and functional properties of tumour vasculature from tumour onset until late-stage disease, a prerequisite for this study was a slow-growing tumour model. Pilot experiments identified these cells as an ideal model for an invasive, slow-growing non-disseminating tumour (Fig. 1) as identified by whole body fluorescent scan (data not shown). Functional and morphological vascular parameters were monitored using fluorescence microscopy. Pre-existing vessels were monitored on days 1, 4, 8 and 12 after tumour cell implantation, and tumour vessels were monitored on days 13, 25, 37, 49, 61 and 85 after tumour cell implantation. As controls cranial windows were implanted in 12-week-old, male, SCID mice without tumour cell implantation and monitored cranial vessels on days 1, 4, 8, 12, 37 and 49. To distinguish between surgery-related alterations and tumour-cell-related alterations, the cover-slip was removed in the control group after day 49 and implanted a cell suspension of 0.5×10^6 HBMEC-1 cells in 4 μl of nutrition media and monitored vascular parameters on days 1, 4, 8 and 12 after tumour cell implantation. All animal procedures were performed according to the German animal welfare committee under assurance number 57/00 (Behörde für Wissenschaft und Gesundheit, Hansestadt Hamburg, Germany).

2.2. Microvascular parameters

2.2.1. Vessel density (VD), vessel volume per area (Vol.p.A), tissue perfusion rate (TPR), blood flow velocity (V_{RBC} and blood flow rate (BFR)

During each observation period, 100 μl of fluorescein isothiocyanate (FITC)-/tetramethylrhodamine isothiocy-

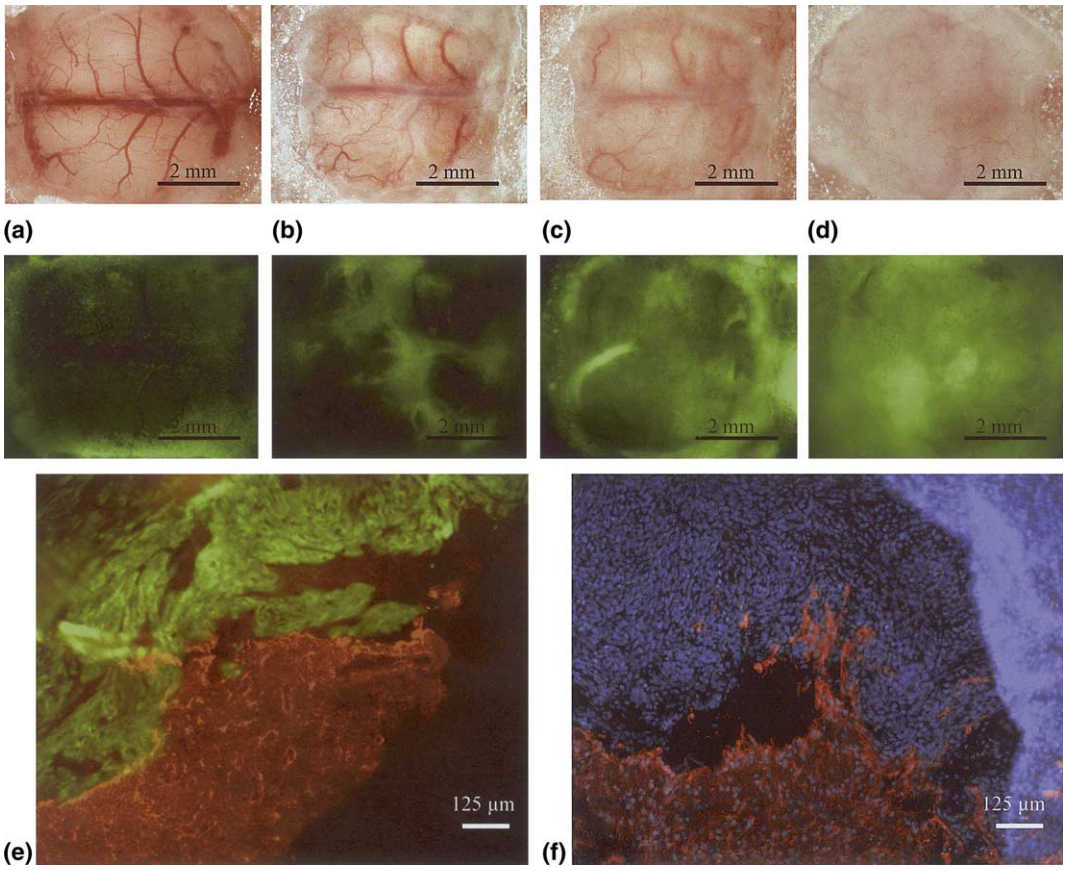

Fig. 1. (a)–(d) Macroscopic aspects of native (upper lane) and fluorescent (lower lane) monitored tumour growth (bar = 2 mm). (a) Directly after tumour cell implantation (day 0), hemispheres and the typical microvascular anatomy including the mid-lined sagittal sinus can be visualised. The fluorescent image shows that tumour cells attach predominantly to the periphery. (b) and (c) Tumour growth until (b) day 13 showed incomplete covering of cranial surface, followed by subsequent complete covering of the cranial surface around (c) day 35. (d) Further tumour growth until day 85 was characterised by increasing tumour volume confirmed by semi-quantitative increasing fluorescence intensity. To avoid neurological symptoms due to the progressive tumour growth, day 85 was chosen as the last observation day. (e) Glial fibrillary acid protein/tetramethylrhodamine isothiocyanate (GFAP/TRITC) immunohistochemistry revealed the invasive tumour growth, showing the tumour (green) invading the brain (red). (f) Nuclei staining with 4′,6-diamidino-2-phenylindole (DAPI) (blue) confirmed the invasive tumour growth, showing the enriched nuclei density in the tumour mass, while nuclei density in the brain (red) was normally distributed.

anate (TRITC)-Dextran (mol. wt. 2×10^6 kDa, 10 mg/ml, Sigma, St. Louis, MO, United States of America (USA)) was injected through the tail vein in order to visualise functional vessels. Fluorescence images were recorded digitally and non-compressed for 20 s in five distinct regions and analysed off-line. Using an image processing system (National Institutes of Health (NIH) Image 1.62), vessel diameter and length were measured to calculate the capillary density, defined as total length of vessels per unit area (cm/cm^2, and the vessel volume per area. The vascular volume was calculated based on diameter (D), length (L) and total number of vessels (M) in the region with the area A: $\text{Vol.p.A} = \pi/4A\sum^{M} i = 1D_i^2 L_i$. The tissue perfusion rate was obtained using vascular density (VD), blood flow rate (BFR) and surface area. The equation to calculate tissue perfusion rate (TPR) is as follows: $\text{TPR}(x) = \frac{1}{G}\sum_{x=1}^{G}\left(\frac{\pi}{4A}\sum_{n=1}^{z} D_n^2 \bullet \frac{1}{\alpha}\text{RBC}_{\text{mean}}\right)_x$, where G is the count of observation fields, the observed surface area, z number of vessels counted in the observed area, α parameter to calculate the ratio between RBC and plasma. Blood flow velocity (V_{RBC}) was measured opto-electronically using a two-slit method (Exbem 3.0, Pixlock). The mean blood flow rate of individual vessels (Q) was calculated using the vessel diameter (D) and the mean blood flow velocity (V_{mean}): $Q = \pi/4 \times V_{\text{mean}} \times D^2$, $V_{\text{mean}} = V_{\text{RBC}}/\alpha\,(\alpha) = 1.3$, for blood vessels <10 µm; linear extrapolation $1.3<\alpha<1.6$ for blood vessels >10 and <15 µm; and $\alpha = 1.6$ for blood vessels >15 µm) [25,26].

2.2.2. Microvascular permeability

Effective microvascular permeability (P) was measured as described previously [1,26]. Briefly, after the injection of TRITC-labelled bovine serum albumin (TRITC-BSA, mol. wt 67,000; excitation wavelength 525–555 nm, emission wavelength 580–635 nm, Molecular Probes, Eugene, OR, USA) (10 mg/ml, 0.1 ml/25 g body weight) the fluorescence intensity was measured intermittently for 25 min and recorded digitally

(PowerLab/200 ADInstruments Pty Ltd., Unit 6, Castle Hill, NSW 2154, Australia). The value of P was calculated as $P = (1-\mathrm{HT})V/S\{1/(I_0-I_b)*\mathrm{d}I/\mathrm{d}t + 1/K\}$, where I is the average fluorescence intensity of the whole image, I_0 is the value of I immediately after the filling of all vessels by TRITC-BSA and I_b is the background fluorescence intensity. The average haematocrit (HT) of vessels is assumed to be equal to 19% [27]. V and S are the total volume and surface area of vessels within the tissue volume covered by the surface image. The time constant of BSA plasma clearance (K) is 9.1×10^3 s [28].

2.3. Leucocyte–endothelial interaction (LEI)

Leucocyte–endothelial interactions in vessels were monitored as described previously [26,29]. Briefly, mice were injected intravenously with a bolus (20 μl) of 0.1% rhodamine-6G in 0.9% saline and leucocytes were visualised via an intensified CCD camera and recorded non-compressed digitally on a computer (Apple Power MacIntosh, G4, Dual 500 MHz Power PC, 1GB SDRAM). The numbers of rolling (Nr) and adhering (Na) leucocytes were counted for 30 s along a 100 μm segment of a vessel. Rolling was defined as a slow movement along the vessel wall (< 50% of V_{RBC}), whereas adhering was defined as a stable position at the vessel wall for 30 s. The total flux of cells for 30 s was also measured (Nt). The total leucocyte flux was normalised by the cross-sectional area of the individual vessel: leucocyte flux (cells/mm^{2}s) = $10^6 \times Nt/(\pi \times (D/2)^2 \times 30\ \mathrm{s})$. Rolling count, the ratio of rolling leucocytes (Nr) to total cell flux (Nt) was calculated as follows: rolling count (%) = $100 \times \mathrm{Nr/Nt}$. The mean leucocyte adhesion at the vessel wall was calculated by normalising the vessel surface area. Adhesion density (cells/mm^2) = $10^6 \times \mathrm{Na}/(\pi \times D \times 100\ \mu\mathrm{m})$. Shear rate of individual blood vessels was measured to determine the forces of blood flow influencing the interactions of leucocytes and endothelium. Shear rate was calculated according to the following equation: Shear rate (s^{-1}) = $8 \times V_{mean}/D$.

2.4. Branching pattern

To investigate the vascular network, five distinct observation areas were analysed for their microvascular architecture [18,19]. Briefly, the vascular network was visualised by fluorescence microscopy after injection of 100 μl of TRITC-Dextran (mol. wt 2×10^6 kDa, 10 mg/ml, Sigma, St. Louis, MO, USA) through the tail vein. The functional vessels were analysed by the following criteria:

1. Numbers of true-loops and self-loops.
2. The mean feeding/draining vessel was assigned to order 1.
3. Daughter vessels were assigned to the next higher order if they diverged at an outside angle of less than 160°.
4. Length and diameter were measured corresponding to vessel order.
5. Outside of loops: numbers of bifurcations and trifurcations.

Self-loops are described as a bifurcation and reunion of the identical vessel without further branching in between retaining the assigned order. Similar to self-loops, true-loops originate from bifurcation and reunion of a vessel with at least one additional branching. All vessels in a true-loop and branches are assigned to the order of the feeding vessel if the rules for a daughter vessel do not apply (see rule 3.) [18,19].

2.5. Scanning electron microscopy

For scanning electron microscopy, the tissue was perfused with phosphate-buffered saline to eliminate all corpuscular parts in the vessel lumen. The tumours were removed, immersed in 2.5% glutaraldehyde (Sigma–Aldrich, Germany) for a minimum of 20 min and embedded in paraffin wax after dehydration in alcohol. The luminal surface of tumour vessels were exposed by cutting microtome sections of 500 μm. Paraffin wax was removed by incubation in 80 °C for 15 min and followed by immersion in xylol, ethanol and acetone. After critical-point-drying (BalTec CPD 030) the sections were sputter-coated with gold (Cressington Sputter Coater, Watford, UK) [30]. Images were taken with a scanning electron microscope (Leo Electron Microscopy Ltd., Cambridge, UK).

2.6. Immunohistochemistry

Mouse brains were removed from the cranial cavity and fixed overnight in paraformaldehyde. Following an ascending sucrose-gradient (7% and 15%, 3 h each and 30% overnight) tumours were embedded in optimum cutting temperature (OCT) embedding compound (Tissue Tek, Elkhart, IN, USA) and stored at −80 °C. For immunohistochemistry, frozen sections (10-μm thick) were fixed in acetone for 90 s prior to staining.

Glial fibrillary acid protein (GFAP) immunohistochemistry was performed to stain the invaded brain. Briefly, the slides were blocked with swine serum (1:10; DAKO, Denmark) for 30 min and incubated with the polyclonal primary rabbit-anti-cow antibody against GFAP (DAKO) at a 1:50 dilution for 40 min. Bound antibody was detected using a tetramethylrhodamine isothiocyanate (TRITC)-labelled swine-anti-rabbit antibody (DAKO) at a 1:30 dilution. The nuclei were counter-stained by incubation with 4′,6-diamidino-2-phenylindole (DAPI) (2 μg/ml) for 15 min.

2.7. Statistical analysis

The results are presented as means ± standard error of the mean (SEM). Statistical analysis was performed with StatView® (Abacus, Berkely, CA, USA) using the Mann–Whitney *U* test for comparison of vascular parameters between tumour and control group. For statistical comparison of paired parameters during the observation period, the Wilcoxon signed-rank test was performed. Statistical significance was based on *P* values smaller than 5%.

3. Results

3.1. Microvascular parameters in pre-existing vessels

3.1.1. Permeability

Subsequent to the surgical intervention of cranial window implantation, the effective microvascular permeability (*P*) decreased significantly in the absence of tumour cells from day 1 to day 8, and further from day 12 to day 37 after cranial window implantation. In contrast, tumour cell implantation was accompanied by an immediate and significant increase in *P*. Although the peak of microvascular permeability was measured on day 12, the relative increase in *P* was pronounced during the first 4 days after tumour cell implantation (Fig. 2(a) and Table 1).

3.1.2. Leucocyte–endothelial interaction

In contrast to the constant rolling count (RC) in the absence of tumour cells, a significant longitudinal increase was found in the RC in the presence of tumour cells in pre-existing vessels (Fig. 2(b) and Table 1). Parallel to the increased RC, tumour cell implantation was associated with significantly increased cell adhesion in pre-existing vessels compared with the control (Table 1). Shear rate decreased significantly in the presence of tumour cells. In the absence of tumour cells, shear rate remained at constant levels (Table 1). No significant longitudinal increase in leucocyte flux in pre-existing vessels was observed, in either the presence or the absence of tumour cells (Table 1).

3.1.3. Vessel density

Although not significant, vessel density of pre-existing vessels initially decreased slightly after tumour cell implantation, whereas the control group without tumour cells was characterised by a slight increase in vessel density (VD) (Table 1).

3.1.4. Vessel diameter

Tumour cell implantation was accompanied by significant vessel dilation. Vessel diameter (*D*) increased continuously from day 1 to day 8 with no further increase on day 12. Vessel diameter in the absence of tumour cells remained constant (Table 1).

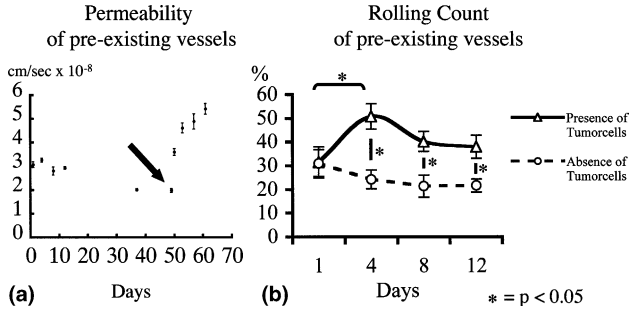

Fig. 2. Directly after surgery permeability was elevated for 12 days and decreased to constant levels from day 12 to day 37. A significant decrease in *P* was found 8 and 37 days after cranial window implantation. Tumour cell implantation (arrow) was accompanied by an immediate and significant increase in *P*. Although it peaked 12 days after tumour cell implantation (day 62), the increase was significantly pronounced during the first 4 days. On all corresponding days in the absence and presence of tumour cells pre-existing vessels revealed significant differences of functional permeability. All values are presented as mean ± SEM ($^{*}P < 0.05$). (b) By labelling leucocyte with rhodamin-6-G, a significant longitudinal increase in rolling leucocytes (rolling count, RC) in the presence of tumour cells was identified in pre-existing vessels from day 1 to day 4. By contrast, the RC in the absence of tumour cells remained unaltered, with only a slight decrease from day 1 to day 4. On day 4, 8 and 12, the presence of tumour cells lead to a significant elevation of the rolling count compared with the control group in the absence of tumour cells. All values are presented as means ± SEM ($^{*}P < 0.05$; $^{*}P = 0.056$) (b).

3.2. Microcirculatory parameters in tumour vessels

3.2.1. Permeability

Permeability of tumour vessels increased significantly from day 13 until day 61. Permeability reached a plateau phase subsequently to day 61 with no further increase until day 85, the end of the observation period (Fig. 3(b) and Table 1).

3.2.2. Vessel density, vessel volume per area

VD in tumours increased significantly from day 13 to day 25, to day 37, with a subsequent plateau phase. In contrast to the unvarying vessel density following day 37, analysis of the vessel volume per area (Vol.p.A) revealed a significant progression until the end of the observation period (Fig. 4(a) and Table 1).

3.2.3. Blood flow rate (BFR)

BFR, representing the individual vessel perfusion dependent on vessel diameter and blood flow velocity (V_{RBC}), remained constant during the early tumour growth phase until day 25. With an invariable vessel diameter until day 49, BFR significantly ($P = 0.014$) increased from day 25 to day 37 due to the increase in V_{RBC}. Increasing diameter of tumour vessels starting from day 49, augment BFR significantly ($P<0.0001$)

Table 1
Microvascular parameters in pre-existing vessels without tumour cell implantation (control group; top), in pre-existing (cranial) vessels in presence of tumour cells (middle) and in tumour vessels (bottom)

Day	1	4	8	12	37	49
Pre-existing vessels, absence of tumor cells (control)						
Permeability ($\times 10^{-8}$ cm/s)	3.07 ± 0.12 (6; 1)	3.25 ± 0.08 (6; 1)	2.79 ± 0.17 (6; 1)	2.92 ± 0.06 (6; 1)	2.00 ± 0.05 (6; 1)	1.97 ± 0.07 (6; 1)
Density (cm/cm^2)	141.38 ± 4.99 (6; 5)	154.57 ± 6.16 (6; 5)	160.37 ± 8.08 (6; 5)	184.15 ± 6.42 (6; 5)	282.92 ± 15.73 (8; 5)	268.71 ± 10.57 (6; 5)
Diameter (μm)	12.88 ± 0.43 (6; 5)	13.55 ± 0.34 (6; 5)	11.32 ± 0.64 (6; 5)	11.00 ± 0.49 (6; 5)	8.91 ± 0.24 (8; 5)	8.51 ± 0.35 (6; 5)
Rolling count (%)	31.10 ± 5.75 (6; 4)	24.24 ± 3.96 (6; 4)	21.40 ± 4.64 (6; 4)	21.65 ± 2.75 (6; 4)	24.98 ± 1.99 (6; 5)	22.28 ± 2.98 (6; 5)
Cell adhesion (cells/mm^2)	23.07 ± 7.11 (6; 4)	38.30 ± 11.52 (6; 4)	83.34 ± 32.10 (6; 4)	13.12 ± 8.14 (6; 4)	12.48 ± 7.6 (6; 5)	12.49 ± 7.25 (6; 5)
Flux (cells/s/μm^2)	1309.45 ± 278.81 (6; 4)	1080.79 ± 295.68 (6; 4)	834.00 ± 152.75 (6; 4)	1085.97 ± 242.62 (6; 4)	1196.31 ± 142.72 (6; 5)	822.39 ± 99.84 (6; 5)
Shear rate (1/s)	404.44 ± 40.86 (6; 1)	334.66 ± 31.89 (6; 1)	343.34 ± 20.23 (6; 1)	378.97 ± 25.39 (6; 1)	Not measured	Not measured

Day	1	4	8	12
Pre-existing vessels, presence of tumor cells				
Permeability ($\times 10^{-8}$ cm/s)	3.59 ± 0.14 (12; 1)	4.61 ± 0.21 (6; 1)	4.87 ± 0.33 (6; 1)	5.41 ± 0.23 (6; 1)
Vessel density (cm/cm^2)	137.02 ± 8.77 (6; 5)	126.63 ± 6.26 (6; 5)	113.51 ± 10.82 (6; 5)	116.60 ± 9.61 (6; 5)
Diameter (μm)	15.76 ± 0.75 (6; 5)	19.66 ± 0.96 (6; 5)	21.44 ± 1.78 (6; 5)	21.43 ± 1.43 (6; 5)
Rolling count (%)	31.42 ± 6.53 (6; 4)	50.84 ± 5.27 (6; 4)	40.21 ± 4.20 (6; 4)	37.94+A4.89 (6; 4)
Cell adhesion (cells/mm^2)	116.59 ± 31.70 (6; 4)	41.17 ± 19.02 (6; 4)	58.84 ± 20.89 (6; 4)	73.21 ± 19.17 (6; 4)
Flux (cells/s/μm^2)	1572.81 ± 296.66 (6; 4)	1142.93 ± 155.79 (6; 4)	1240.92 ± 201.44 (6; 4)	920.25 ± 109.07 (6; 4)
Shear rate (1/s)	295.18 ± 43.57 (6; 3)	192.79 ± 29.45 (6; 3)	207.76 ± 26.19 (6; 3)	207.94 ± 26.54 (5; 3)

Day	13	25	37	49	61	85
Tumor vessels						
Permeability ($\times 10^{-8}$ cm/s)	2.52 ± 0.07 (15; 1)	2.66 ± 0.07 (13; 1)	3.15 ± 0.11 (14; 1)	3.75 ± 0.15 (12; 1)	4.34 ± 0.25 (10; 1)	4.24 ± 0.35 (5; 1)
Vessel density (cm/cm^2)	67.55 ± 3.02 (15; 5)	80.10 ± 4.92 (13; 5)	114.98 ± 7.90 (14; 5)	119.66 ± 7.46 (12; 5)	114.24 ± 5.09 (10; 5)	131.61 ± 9.31 (5; 5)
Diameter (μm)	9.94 ± 0.17 (15; 4)	10.01 ± 0.18 (13; 4)	10.82 ± 0.26 (14; 4)	13.48 ± 0.50 (12; 4)	13.38 ± 0.36 (10; 4)	12.86 ± 0.33 (5; 4)
Volume p.A. (μm^3/μm^2)	0.86 ± 0.07 (15; 5)	1.06 ± 0.09 (13; 5)	1.87 ± 0.18 (14; 5)	2.91 ± 0.27 (12; 5)	3.41 ± 0.21 (10; 5)	3.96 ± 0.65 (5; 5)
Rolling count (%)	34.8 ± 3.81 (15; 4)	41.02 ± 4.06 (12; 4)	48.87 ± 2.95 (14; 4)	48.39 ± 2.64 (11; 4)	53.56 ± 1.47 (10; 4)	46.62 ± 3.62 (5; 4)
Cell adhesion (cells/mm^2)	29.91 ± 11.73 (15; 4)	34.09 ± 12.77 (12; 4)	36.23 ± 12.85 (14; 4)	45.02 ± 14.34 (11; 4)	99.62 ± 24.1 (10; 4)	202 ± 83.23 (5; 4)
Flux (cells/s/μm^2)	1241.16 ± 174.51 (15; 4)	1708.88 ± 239.86 (12; 4)	1525.82 ± 133.01 (14; 4)	1051.12 ± 71.34 (11; 4)	846.01 ± 111.76 (10; 4)	795.9 ± 126.3 (5; 4)
Shear rate (1/s)	213.86 ± 39.37 (6; 4)	215.89 ± 30.43 (6; 4)	204.62 ± 48.27 (14; 4)	144.55 ± 13.45 (5; 4)	125.3 ± 8.9 (6; 4)	97.11 ± 13.51 (5; 4)
BFR ($\times 10^4$ μm^3/s)	1.86 ± 0.08 (6; 5)	2.23 ± 0.12 (6; 5)	2.95 ± 0.26 (6; 5)	5.40 ± 0.63 (5; 5)	4.20 ± 0.30 (6; 5)	3.50 ± 0.24 (5; 5)
TPR ($\times 10^{-5}$ ml/cm^2/s)	14.6 ± 1.46 (6; 5)	20.0 ± 1.9 (6; 5)	37.5 ± 10.1 (6; 5)	46.1 ± 9.6 (6; 5)	52.4 ± 7.34 (6; 5)	42.4 ± 4.2 (5; 5)
Vrbc ($\times 10^{-1}$ μm/s)	31.25 ± 0.96 (6; 4)	35.46 ± 1.04 (6; 4)	38.69 ± 1.05 (6; 4)	38.47 ± 1.03 (5; 4)	34.75 ± 0.89 (6; 4)	31.15 ± 0.82 (5; 4)
Caliber variation p.A.	0.51 ± 0.17 (6; 5)	0.87 ± 0.17 (6; 5)	0.72 ± 0.07 (6; 5)	0.99 ± 0.24 (6; 5)	1.37 ± 0.29 (6; 5)	1.36 ± 0.39 (5; 5)
Trueloops p.A.	0.46 ± 0.10 (6; 5)	0.30 ± 0.12 (6; 5)	0.30 ± 0.10 (6; 5)	0.54 ± 0.05 (6; 5)	0.50 ± 0.09 (6; 5)	0.68 ± 0.17 (5; 5)
Selfloops p.A.	0.17 ± 0.07 (6; 5)	0.16 ± 0.07 (5; 5)	0.13 ± 0.06 (6; 5)	0.03 ± 0.03 (6; 5)	0.16 ± 0.04 (5; 5)	0.28 ± 0.09 (5; 5)
Trifurcation p.A.	0.10 ± 0.06 (6; 5)	0.23 ± 0.09 (6; 5)	0.43 ± 0.13 (6; 5)	0.34 ± 0.15 (6; 5)	0.47 ± 0.10 (6; 5)	0.72 ± 0.12 (5; 5)
Bifurcation p.A.	2.48 ± 0.33 (6; 5)	3.03 ± 0.45 (6; 5)	3.71 ± 0.52 (6; 5)	3.51 ± 0.34 (6; 5)	3.87 ± 0.21 (6; 5)	3.72 ± 0.48 (5; 5)

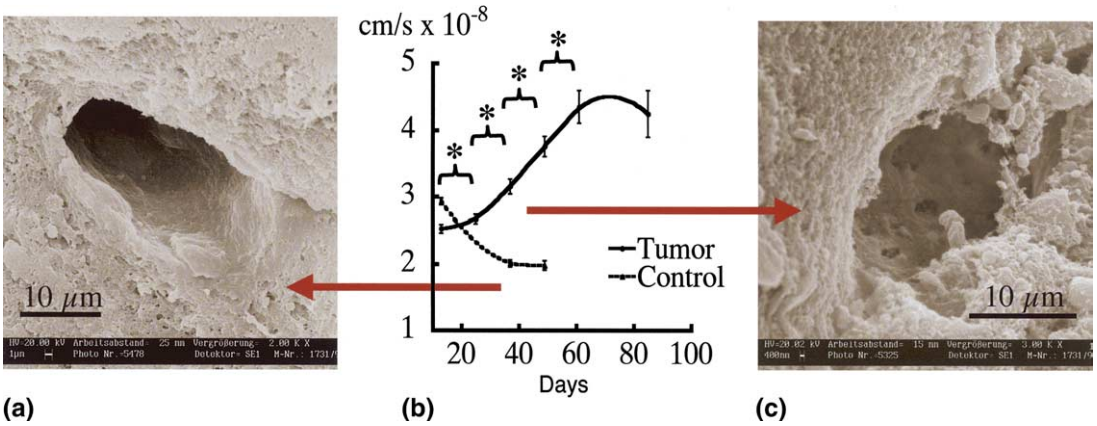

Fig. 3. (a) Representative image of normal vessels in the cranium, demonstrating the laminar structure and closed endothelial lining with prominent nuclei. (b) Tumour vessels demonstrated a significant increase in permeability from day 13 to day 62. No further increase until the end of observation period was observed. From day 37 onward tumour vessels revealed a significant elevation of permeability than control vessels in the cranial window. All values are presented as means ± SEM ($^{*}P < 0.05$). (c) Representative image of early staged tumour vessels with thin endothelial lining and multiple gaps (arrow) but without inner luminal bridging and irregularities. Number and size of gaps in the endothelial lining might correlate with increased effective microvascular permeability. *, significant P-values <0.05.

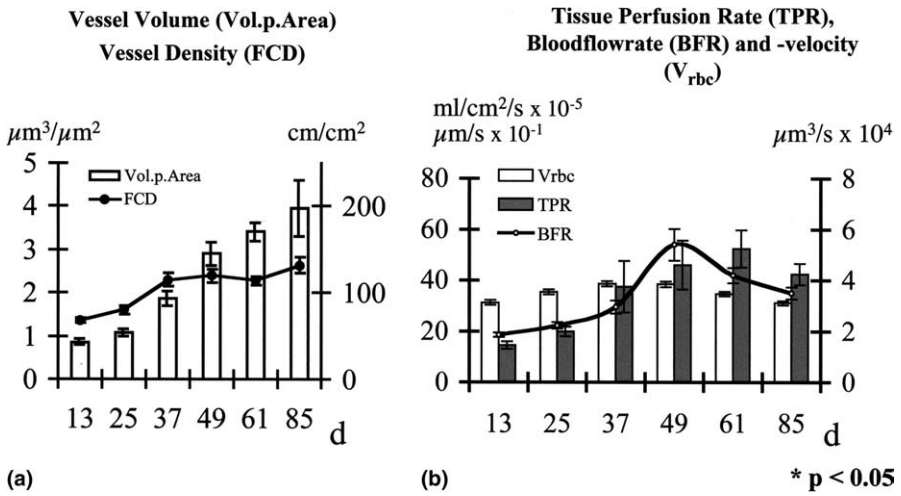

Fig. 4. (a) Functional capillary density (FCD) and volume per observation area (A) was measured in tumour vessels on days 13, 25, 37, 49, 61 and day 85. FCD increased significantly from day 13 to day 25 to day 37 then reached a steady sate. In contrast to the constant FCD, volume per area increased continuously beyond day 37 due to the growing vessel diameter. All values are presented as mean ± SEM ($^{*}P < 0.05$). (b) Increase in TPR was observed from tumour onset until day 62, though the increase between individual observation days was only significant from day 13 to day 25 and from day 25 to day 49. A slight, non-significant decrease in TPR was observed on day 85. All values are presented as means ± SEM ($^{*}P < 0.05$).

from day 37 to day 49. After the peak on day 49, BFR decreased to 4.1 $\mu m^3/s \times 10^4$ on day 61 and to 3.5 $\mu m^3/s \times 10^4$ on day 85 (Fig. 4(b) and Table 1).

3.2.4. Tissue perfusion rate

Similar to the single vessel perfusion parameter (BFR), TPR increased predominantly during early tumour growth phase, while later stages were characterised by a steady state. In contrast to BFR, TPR peaked on day 61 and slightly decreased until day 85 (Fig. 4(b) and Table 1).

3.2.5. Vessel diameter, red blood cell velocity

Mean vessel diameter (D) of tumour vessels increased significantly ($P = 0.01$) from day 13 to day 85 (Table 1). This increase was mainly due to a reduction in small capillaries ranging from 4 to 12 μm, while the count of vessels larger than 16 μm increased constantly with tumour ageing ($P = 0.052$; Kruskal–Wallis test) (Fig. 5). Despite the increasing diameter, V_{RBC} slightly, although not significantly, increased from day 13 to day 49 (Fig. 4(b) and Table 1).

3.2.6. Leucocyte–endothelial interaction

Tumour vessels demonstrated a significantly increased RC until day 61, further tumour progression was characterised by a stable RC (Fig. 6(b) and Table 1). RC in the control group remained at a constant level (Fig. 6(b) and Table 1). Correspondent to these functional alterations of LEI, morphological alterations to

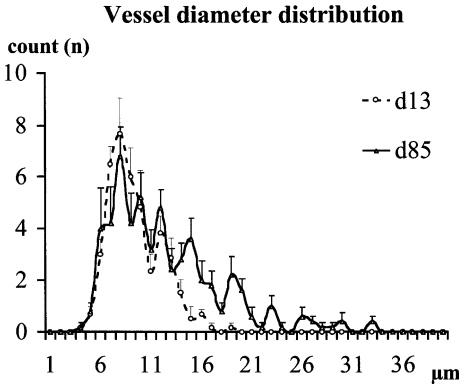

Fig. 5. Analysis of vessel diameter distribution reveals that, with tumour progression, the increase in vessel diameter is due to a reduction in small vessels with diameters <12 µm and a simultaneous increase in vessels with diameters >16 µm. The reduction in small vessels might help to explain the heterogeneous tissue oxygenation due to the limitation of oxygen diffusion distance to about 100 µm.

the ultrastructure were detected by scanning electron microscopy. Irregular intraluminal lining and transluminal bridging increased with tumour ageing (Fig. 6(c)) compared with regular lining of control vessels (Fig. 6(a)). In contrast to RC, cell adhesion in tumour vessels increased only slightly until day 49 followed by a relevant elevation on day 61 ($P = 0.05$), and a further significant expansion on day 85 (Table 1). The shear rate in tumour vessels remained constant until day 37, followed by a decrease on day 49 and a subsequent reduction until day 85 (Table 1). Leucocyte flux in tumour vessels was characterised by an extraneous elevation until day 25. In the sequel insignificantly decreasing numbers of floating leucocytes were observed, reaching a steady state on day 61 (Table 1).

3.3. Tumour vessel characterisation

The 100% variation in vessel calibre demonstrated a positive trend from day 13 to day 61 ($P = 0.068$) (Figs. 7(a), 8(b) and Table 1). The number of bifurcations per area increased significantly from day 25 to day 37 and remained constant at a significantly elevated level (Fig. 7(c) and Table 1). The number of trifurcations increased significantly during the observation period (Fig. 7(d) and Table 1). Note that the increase is 7.2-fold for trifurcations instead of 1.45-fold for bifurcations, reflecting the pathological vessel-splitting pattern in tumours. Although not significant, it was noticeable that the number of true- and self-loops increased with tumour progression (Figs. 7(b) and 8(c) and (d)). Tumour vessels assigned to order 1 were characterised by a mean diameter of 13.53 ± 0.54 µm on day 13, whereas diameter of vessels assigned to the next higher order decreased continuously (range 12.2 ± 0.26 µm (order 2) to 9.68 ± 0.96 µm (order 5)). In the sequel, the diameter

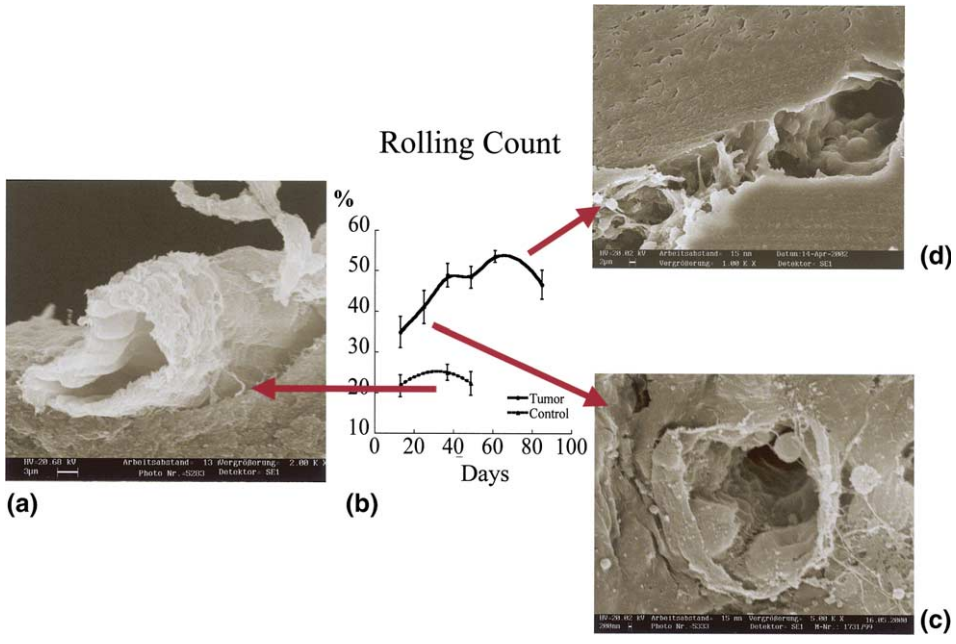

Fig. 6. (a) Representative ultrastructure of a regular vessel in the cranium with laminar architecture of the harmonious vessel wall, closed endothelial lining and prominent nuclei. (b) Quantitative analysis of rolling count (RC) at the vessel wall of tumour and control vessels in the cranium. Tumour vessels demonstrated a significant increase in RC predominantly during the first 37 days. Although RC from thereafter increased with tumour progression this increase was not significant. The RC in the control group was unaltered. During all observation days the RC differed significantly between control and tumour vessels. All values are presented as means ± SEM ($^{*}P < 0.05$). (c) Representative ultrastructure of an early stage tumour vessel with thin endothelial lining yet with regular surface and prominent endothelial cells. (d) Representative ultrastructure of a late-stage tumour vessel in the cranium with thin and irregular lining, multiple gaps and transluminal bridging.

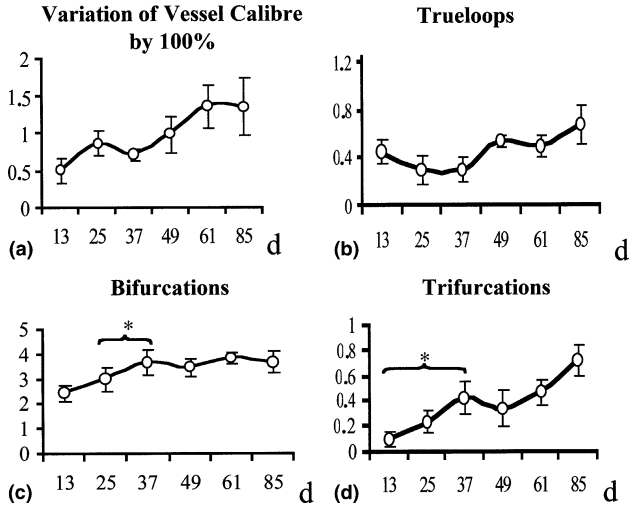

Fig. 7. (a) The variation in vessel calibre by >100% increased from day 13 until day 61. Although this increase was only a trend ($P = 0.068$), it represents the development of pathological vessel diameter variation leading to irregular blood flow as described in late-stage tumour vascularisation. (b) The minimal number of true-loops per area was found on day 25 with an increase to a maximum on day 85. (c) The number of bifurcations per area increased significantly from day 25 to day 37 and remained constant at a significantly elevated level thereafter. (d) The number of trifurcations increased significantly from day 13 until day 37, later increases were not significant between subsequent days. Note that the percentage increase is 7.2-fold for trifurcations instead of 1.45-fold for bifurcations, reflecting the pathological vessel splitting.

of vessels assigned to order 1 increased to a mean of 23.34 ± 1.23 μm until day 85. Vessels assigned to order 2 or higher appeared similar in their diameter at the end of observation (14.94 ± 2.97 to 17.7 μm). The length of vessels assigned to order 1 remained constant from day 13 (95.87 ± 4.1 μm) to day 85 (92.85 ± 6.42 μm). On day 13, vessels assigned to order 2, 3, 4, 5 and 6 are found on a lower but constant level (72.35 ± 3.25 to 56.46 ± 7.84 μm). From start to end of the observation period vessels assigned to order 2 increased in length. On day 85 they demonstrated similar lengths as vessels of order 1 (92.85 ± 6.42 μm, order 2: 96.54 ± 12.93 μm).

3.4. Immunhistochemistry

Glial fribrillary acid protein (GFAP)-staining showed brain-invasive tumour growth (Fig. 1(e) and (f)).

3.5. Scanning electron microscopy

Control vessels in the cranial window were characterised by a regular endothelial surface (Figs. 3(a) and 6(a)). One day after tumour cell implantation, distinct alterations could be detected corresponding to openings within the endothelium and prominent nuclei of the endothelial cells (Fig. 3(c)). Day 12 in the presence of tumour cells did not show further alterations after day 1. Tumour vessels revealed intraluminal abnormalities such as multiple intercellular openings and transluminal bridging at the end of observation (Fig. 6(c)). Tumour vessels are also irregular during tumour onset (day 37), but these characteristics appeared less marked.

4. Discussion

Functional and morphological dynamics of the multifaceted process of tumour angiogenesis have been reported here, from stimulation of pre-existing host vessels during tumour onset to the characteristics of tumour microcirculation during late-stage tumour disease. Fluorescence microscopy, using a cranial window preparation, allows long-term monitoring of morphological and, especially, functional alterations. It, therefore, permits insights into functional vascular properties and their morphological correlate in tumour microcirculation *in vivo* [31]. These data corroborate the finding that tumour angiogenesis is a multi-step process with step-specific characteristics of the tumour vasculature, implying that step-specific therapeutic strategies are required to exploit vascular properties to optimal therapeutic effect [13,32,33].

4.1. Pre-existing vessels

Increased microvascular permeability and vessel dilatation belong to the initial steps of angiogenesis, followed by extracellular matrix degradation and endothelial proliferation [12]. Consequently, the initially altered functional parameter was the significantly increased microvascular permeability of pre-existing host vessels. The extent of this augmented permeability was considerably beyond that provoked by surgical intervention in the absence of tumour cells (Fig. 1(a)). The morphological correlate to the increased permeability was an increased pore size, as identified by scanning electron microscopy (Figs. 2(b) and 4(b)), suggesting a facilitated transendothelial transport for therapies based on high molecular weight substrates [34]. While the abrupt and substantial reaction to tumour cell implantation suggests that permeability acts as the most sensitive functional parameter, the initial morphological alteration is a dilatation of the vasculature, with consequently increased blood flow rate. These data identify the initial steps of tumour progression as susceptible to therapies requiring a high perfusion rate, such as conventional chemotherapy [35,36]. The increase in permeability and leucocyte–endothelial interaction (LEI) following surgical intervention support the hypothesis that therapies, such as surgical intervention or radiation therapy might contribute to tumour progression by stimulating the angiogenic vascular endothelial growth factor

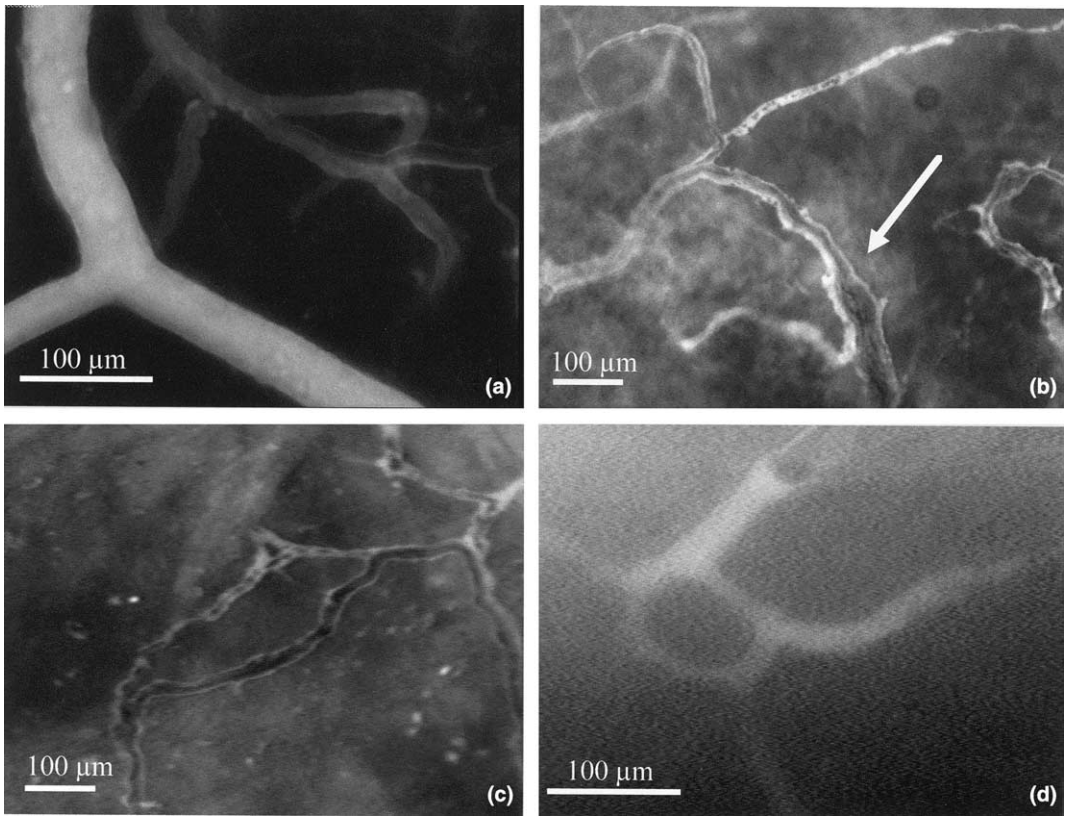

Fig. 8. (a) Regular branching pattern of control vessels in the cranial window producing a non-disturbed laminar blood flow. (b) Tumour vessels are heterogeneously distributed and show variation in calibre by more than 100% (arrow) leading to irregular blood flow. (c) Self-loops (here starting to sprout) and (d) true-loops are pathological vessel formations in tumour tissue. (Bar = 100 μm).

(VEGF)-system [37,38]. Therefore peri-operative therapies decreasing permeability, such as anti-VEGFR-2 (1), or COX-2 inhibitors [39,40] might be beneficial to prevent tumour progression as "side effect" of surgical therapies. The observation that an increase in functional vascular density (VD) after tumour cell implantation lags behind the VD in the control group is likely to be the result of the activated angiogenic VEGF system following surgical intervention [37] in the control group, while tumour implantation is also associated with Angiopoietin-2 expression. The firstly unanticipated reduction in VD of pre-existing vessels after tumour cell implantation might be explained by the mechanism of vessel co-option as a step of tumour angiogenesis, or initial vessel regression mediated by increased levels of angiopoietin-2 [41].

4.2. Tumour vascularisation

Independent from the origin of tumour vascularisation, whether it results from angiogenic, arteriogenic or vasculogenic mechanisms, functional properties of the newly formed vessels govern tumour microenvironment, tumour progression and drug delivery [4,24]. Therefore, it is important to gain insights into the sequential alteration in functional alterations of tumour vessels [12]. Once tumour progression results in neovascularisation, the properties of the newly formed vessels are governed by tumour type and altered by site-specific aspects [12,42].

Microvessel density has been suggested as a useful prognostic indicator to evaluate tumour progression [43,44] but despite the importance as prognostic indicator, microvessel density does not mirror the angiogenic activity or angiogenic dependence of a tumour rather it reflects the metabolic demands of the tumour [11,45,46]. In the model used in this study an increasing capillary density was seen until day 37, followed by a plateau phase. While the capillary sprouting did not further increase after day 37, analysis of the vessel volume revealed a continuous progression due to growing vessel diameter in the continuously expanding tumour. Though the enlargement of vessel diameter might increase tissue perfusion rate, the shift towards bigger vessels occurred at the costs of vessels smaller than 16 μm, contributing to heterogeneous pH and pO_2 profiles due to the limitation of oxygen diffusion to 100 μm [47].

Besides the reduction in small vessels, heterogeneous blood flow velocity associated with the variation in calibre and the pathologic branching pattern such as trifur-

cation, true- and self-loops contribute to local heterogeneity of metabolic parameters [16,18]. Variation in vessel calibre is responsible for disturbances of blood flow up to temporal or permanent stasis [19]. These characteristics, as well as true-loops and self-loops (including self-feeding loops) led to a reduced blood flow rate and contributed to the reduction in tissue perfusion rate at later stages. Self-feeding loops in particular might be responsible for insufficient tissue perfusion and contribute to impaired drug delivery. Bifurcations have to be regarded as non-pathological structures. Their count increased in parallel with the increase in capillary density. In contrast, trifurcations are considered to be pathological structures. Their increase after day 37 might have contributed to the reduction in the tissue perfusion rate. The continuous increase in pathological branching pattern with disorganisation and irregular shape of tumour vessels might also represent the absence of vessel maturing processes.

While the increased permeability of *pre-existing* vessels contributed to the process of angiogenesis the continuous increase in permeability in *tumour vessels* beyond day 37 with a subsequently stable capillary density might represent the functional correlate of a vasculature with absent maturing process. Scanning electron microscopy and functional permeability measurements could identify even large vessels with thin walls and focal intercellular openings contributing to sustained increased microvascular permeability and plasma exsudation [48]. The high levelled but stable permeability at the end of the observation period might mirror the balance between increased vessel leakiness with plasma extravasation and the resulting increased interstitial fluid pressure. This balance between extravasation and convection forces represents an additional barrier to a constant drug delivery [25].

Blood flow and other mechanical parameters affect the delivery of leucocytes and therapeutically applied molecules [49], whereas the biological interaction with the endothelium influences the probability of extravasation [50–52]. Therefore the increased rolling count of leucocytes observed in the model used in this study, might reflect the augmented possibility of cell surfaceendothelial interactions as a result of rheological alterations with heterogeneous blood flow velocity. The irregular endothelial lining with intraluminal bridging analysed by scanning electron microscopy might explain a mechanical promotion of increased LEI via the interruption of laminar blood flow. The constant leucocyte flux could be used to guarantee the absence of inflammatory or immunological reactions. From these results, one can conclude that therapies might benefit from decreased shear rate via increased cell surface interaction, while on the other side pathological heterogeneous distribution might disturb homogeneous therapeutic infiltration [53–56].

Due to the limited sampling depth of intravital fluorescence microscopy, the two-dimensional analysis might not reflect the complex three-dimensional characteristics of tumour vascularisation. A further limitation of general clinical relevance might be the chosen tumour model. However, the focus of the study was on long-term observation of morphological and functional properties of tumour vasculature from tumour onset until late-stage disease, requiring a slow-growing tumour model. An invasive, slow-growing non-disseminating tumour model was, therefore, favoured despite the relatively low clinical relevance of this model.

Taken together, this tumour model enabled the investigation the dynamics of barriers to drug delivery continuously and non-invasively for a period of 3 months. It was demonstrated that tumour cells caused an elevated permeability of host vessels due to increased pore size. Newly perfused vessels were found 3 days and tumour vasculature in solid tumour parts 13 days after tumour cell implantation. This can be utilised for the delivery of macromolecules during tumour onset to target parenchymal and tumour cells, or during current tumour disease to prevent multifocal metastasis by decreasing permeability as the initial step of angiogenesis. The vulnerable tumour onset period is characterised by a regular vascular morphology and branching pattern. Later stages with established tumours and tumour vessels demonstrated an increasing heterogeneous vessel distribution, irregular vessel morphology and branching pattern. As a result, the TPR stagnated in spite of tumour growth and increasing vessel volume and that might lead to impaired drug delivery. Efficiency of adjuvant therapies depends not only on their intrinsic efficiency but also on the timing of their initiation. Therapies depending on the delivery of larger molecules are more efficient during tumour onset, while therapies that equalise blood supply, for example anti-vascular therapies, can be helpful to normalise drug delivery for combined therapies in later stages of tumour growth.

Conflict of interest statement

None declared.

Acknowledgements

This work was supported by a Werner Otto Stiftung research grant to NH-A. NH-A, LW, C.J and C.S are members of the DFG Graduate Kolleg [GRK476], PA is a member of the DFG Graduate Kolleg [GRK336]. The authors thank B. Schwarzloh for outstanding technical support, M. Ammelt for assistance with the image processing analysis, I. Müller for assistance with data analysis and Nancy Morkel for assistance with the manuscript.

References

1. Hansen-Algenstaedt N, Stoll BR, Padera TP, *et al*. Tumor oxygenation in hormone-dependent tumors during vascular endothelial growth factor receptor-2 blockade, hormone ablation, and chemotherapy. *Cancer Res* 2000, **60**(16), 4556–4560.
2. Wyckoff JB, Jones JG, Condeelis JS, *et al*. A critical step in metastasis: *in vivo* analysis of intravasation at the primary tumor. *Cancer Res* 2000, **60**(9), 2504–2511.
3. Paget S. The distribution of secondary growths in cancer of the breast. *Lancet* 1889, **1**, 571–573.
4. Rockwell S. Oxygen delivery: implications for the biology and therapy of solid tumors. *Oncol Res* 1997, **9**(67), 383–390.
5. Jain RK. Delivery of novel therapeutic agents in tumors: physiological barriers and strategies. *J Natl Cancer I* 1989, **81**(8), 570–576.
6. Folkman J. Seminars in Medicine of the Beth Israel Hospital, Boston. Clinical applications of research on angiogenesis. *New Engl J Med* 1995, **333**(26), 1757–1763.
7. Hood JD, Bednarski M, Frausto R, *et al*. Tumor regression by targeted gene delivery to the neovasculature. *Science* 2002, **296**(5577), 2404–2407.
8. Herbst RS, Hess KR, Tran HT, *et al*. Phase I study of recombinant human endostatin in patients with advanced solid tumors. *J Clin Oncol* 2002, **20**(18), 3792–3803.
9. Thomas JP, Arzoomanian RZ, Alberti D, *et al*. Phase I pharmacokinetic and pharmacodynamic study of recombinant human endostatin in patients with advanced solid tumors. *J Clin Oncol* 2003, **21**(2), 223–231.
10. Tseng JE, Glisson BS, Khuri FR, *et al*. Phase II study of the antiangiogenesis agent thalidomide in recurrent or metastatic squamous cell carcinoma of the head and neck. *Cancer* 2001, **92**(9), 2364–2373.
11. Hlatky L, Hahnfeldt P, Folkman J. Clinical application of antiangiogenic therapy: microvessel density, what it does and doesn't tell us. *JNCI Cancer Spectr* 2002, **94**(12), 883–893.
12. Carmeliet P, Jain RK. Angiogenesis in cancer and other diseases. *Nature* 2000, **407**(6801), 249–257.
13. Bergers G, Javaherian K, Lo KM, *et al*. Effects of angiogenesis inhibitors on multistage carcinogenesis in mice. *Science* 1999, **284**(5415), 808–812.
14. Kerbel R, Folkman J. Clinical translation of angiogenesis inhibitors. *Nat Rev Cancer* 2002, **2**(10), 727–739.
15. Chaplin DJ, Olive PL, Durand RE. Intermittent blood flow in a murine tumor: radiobiological effects. *Cancer Res* 1987, **47**(2), 597–601.
16. Helmlinger G, Yuan F, Dellian M, *et al*. Interstitial pH and pO2 gradients in solid tumors *in vivo*: high-resolution measurements reveal a lack of correlation. *Nat Med* 1997, **3**(2), 177–182.
17. Teicher BA. Hypoxia and drug resistance. *Cancer Metast Rev* 1994, **13**(2), 139–168.
18. Less JR, Skalak TC, Sevick EM, *et al*. Microvascular architecture in a mammary carcinoma: branching patterns and vessel dimensions. *Cancer Res* 1991, **51**(1), 265–273.
19. Less JR, Posner MC, Skalak TC, *et al*. Geometric resistance and microvascular network architecture of human colorectal carcinoma. *Microcirculation* 1997, **4**(1), 25–33.
20. Jain RK. Determinants of tumor blood flow: a review. *Cancer Res* 1988, **48**(10), 2641–2658.
21. Jain RK. The Eugene M. Landis Award Lecture 1996. Delivery of molecular and cellular medicine to solid tumors. *Microcirculation* 1997, **4**(1), 1–23.
22. Schweitzer KM, Vicart P, Delouis C, *et al*. Characterization of a newly established human bone marrow endothelial cell line: distinct adhesive properties for hematopoietic progenitors compared with human umbilical vein endothelial cells. *Lab Invest* 1997, **76**(1), 25–36.
23. Duhrsen U, Martinez T, Vohwinkel G, *et al*. Effects of vascular endothelial and platelet-derived growth factor receptor inhibitors on long-term cultures from normal human bone marrow. *Growth Factors* 2001, **19**(1), 1–17.
24. Yuan F, Salehi HA, Boucher Y, *et al*. Vascular permeability and microcirculation of gliomas and mammary carcinomas transplanted in rat and mouse cranial windows. *Cancer Res* 1994, **54**(17), 4564–4568.
25. Leunig M, Yuan F, Menger MD, *et al*. Angiogenesis, microvascular architecture, microhemodynamics, and interstitial fluid pressure during early growth of human adenocarcinoma LS174T in SCID mice. *Cancer Res* 1992, **52**, 6553–6560.
26. Algenstaedt P, Schaefer C, Biermann T, *et al*. Microvascular alterations in diabetic mice correlate with level of hyperglycemia. *Diabetes* 2003, **52**(2), 542–549.
27. Lipowsky HH, Zweifach BW. Applications of the "two-slit photometric technique to the measurement of microvascular volumetric flow rates. *Microvasc Res* 1978, **15**, 93–101.
28. Yuan F, Leunig M, Huang SK, *et al*. Microvascular permeability and interstitial penetration of sterically stabilized (stealth) liposomes in a human tumor xenograft. *Cancer Res* 1994, **54**(13), 3352–3356.
29. Fukumura D, Salehi HA, Witwer B, *et al*. Tumor necrosis factor alpha-induced leukocyte adhesion in normal and tumor vessels: effect of tumor type, transplantation site, and host strain. *Cancer Res* 1995, **55**(21), 4824–4829.
30. Heintz C, Riepe G, Birken L, *et al*. Corroded nitinol wires in explanted aortic endografts: an important mechanism of failure? *J Endovasc Ther* 2001, **8**(3), 248–253.
31. Jain RK, Munn L, Fukumura D. dissecting tumor pathophysiology using intravital microscopy. *Nat Rev Cancer* 2002, **2**, 266–276.
32. Bagley RG, Walter-Yohrling J, Cao X, *et al*. Endothelial precursor cells as a model of tumor endothelium: characterization and comparison with mature endothelial cells. *Cancer Res* 2003, **63**(18), 5866–5873.
33. Bergers G, Benjamin LE. Angiogenesis: tumorigenesis and the angiogenic switch. *Nat Rev Cancer* 2003, **3**(6), 401–410.
34. Monsky WL, Fukumura D, Gohongi T, *et al*. Augmentation of transvascular transport of macromolecules and nanoparticles in tumors using vascular endothelial growth factor. *Cancer Res* 1999, **59**(16), 4129–4135.
35. Kallinowski F, Schlenger KH, Runkel S, *et al*. Blood flow, metabolism, cellular microenvironment, and growth rate of human tumor xenografts. *Cancer Res* 1989, **49**(14), 3759–3764.
36. Baxter LT, Jain RK. Transport of fluid and macromolecules in tumors. III. Role of binding and metabolism. *Microvasc Res* 1991, **41**(1), 5–23.
37. Hansen-Algenstaedt N, Algenstaedt P, Bottcher A. Bilaterally increased VEGF-levels in muscles during experimental unilateral callus distraction. *J Orthop Res* 2003, **21**(5), 805–812.
38. Hartford AC, Gohongi T, Fukumura D, *et al*. Irradiation of a primary tumor, unlike surgical removal, enhances angiogenesis suppression at a distal site: potential role of host-tumor interaction. *Cancer Res* 2000, **60**(8), 2128–2131.
39. Matsumoto H, Ma WG, Daikoku T, *et al*. Cyclooxygenase-2 differentially directs uterine angiogenesis during implantation in mice. *J Biol Chem* 2002, **277**(32), 29260–29267.
40. Chiarugi V, Magnelli L, Gallo O. Cox-2, iNOS and p53 as playmakers of tumor angiogenesis (review. *Int J Mol Med* 1998, **2**(6), 715–719.
41. Holash J, Maisonpierre PC, Compton D, *et al*. Vessel cooption, regression, and growth in tumors mediated by angiopoietins and VEGF. *Science* 1999, **284**(5422), 1994–1998.

42. Keyes KA, Mann L, Teicher B, *et al*. Site-dependent angiogenic cytokine production in human tumor xenografts. *Cytokine* 2003, **21**(2), 98–104.
43. Weidner N, Folkman J. Tumoral vascularity as a prognostic factor in cancer. *Important Adv Oncol*, 167–190.
44. Borre M, Offersen BV, Nerstrom B, *et al*. Microvessel density predicts survival in prostate cancer patients subjected to watchful waiting. *Brit J Cancer* 1998, **78**(7), 940–944.
45. Rubin MA, Buyyounouski M, Bagiella E, *et al*. Microvessel density in prostate cancer: lack of correlation with tumor grade, pathologic stage, and clinical outcome. *Urology* 1999, **53**(3), 542–547.
46. Chapman JD, Engelhardt EL, Stobbe CC, *et al*. Measuring hypoxia and predicting tumor radioresistance with nuclear medicine assays. *Radiother Oncol* 1998, **46**(3), 229–237.
47. Vaupel P, Hutten H, Thews G. Critical diffusion ranges for oxygen and glucose in tumor tissue considering Michaelis–Menten kinetics. *Bibl Anat* 1975, **13**, 313–314.
48. Hashizume H, Baluk P, Morikawa S, *et al*. Openings between defective endothelial cells explain tumor vessel leakiness. *Am J Pathol* 2000, **156**(4), 1363–1380.
49. Jain RK. The next frontier of molecular medicine: delivery of therapeutics. *Nat Med* 1998, **4**(6), 655–657.
50. Jain RK, Koenig GC, Dellian M, *et al*. Leukocyte-endothelial adhesion and angiogenesis in tumors. *Cancer Metast Rev* 1996, **15**(2), 195–204.
51. von Andrian UH, Chambers JD, McEvoy LM, *et al*. Two-step model of leukocyte-endothelial cell interaction in inflammation: distinct roles for LECAM-1 and the leukocyte beta 2 integrins *in vivo*. *Proc Natl Acad Sci USA* 1991, **88**(17), 7538–7542.
52. Lawrence MB, Springer TA. Leukocytes roll on a selectin at physiologic flow rates: distinction from and prerequisite for adhesion through integrins. *Cell* 1991, **65**(5), 859–873.
53. Semino C, Martini L, Queirolo P, *et al*. Adoptive immunotherapy of advanced solid tumors: an eight year clinical experience. *Anticancer Res* 1999, **19**(6C), 5645–5649.
54. Schiltz PM, Beutel LD, Nayak SK, *et al*. Characterization of tumor-infiltrating lymphocytes derived from human tumors for use as adoptive immunotherapy of cancer. *J Immunother* 1997, **20**(5), 377–386.
55. Irjala H, Salmi M, Alanen K, *et al*. Vascular adhesion protein 1 mediates binding of immunotherapeutic effector cells to tumor endothelium. *J Immunol* 2001, **166**(11), 6937–6943.
56. Silberstein DS, Schoof DD, Rodrick ML, *et al*. Activation of eosinophils in cancer patients treated with IL-2 and IL-2-generated lymphokine-activated killer cells. *J Immunol* 1989, **142**(6), 2162–2167.